Seismic collapse fragility of low-rise steel moment frames with mass irregularity based on shaking table test

Yongtao Bai[1,2], Yinsheng Li[3], Zhenyun Tang[4], Marius Bittner[5], Matteo Broggi[5], and Michael Beer[5,6,7]

1 *Institute of Engineering Mechanics, China Earthquake Administration*

2 *School of Civil Engineering, Chongqing University, Chongqing 400044, China*

3 *Department of Civil Engineering, Xi'an Jiaotong University, 710049 Xi'an, China.*

4 *The Key Laboratory of Urban Security and Disaster Engineering of Ministry of Education, Beijing University of Technology. Email: zyt@bjut.edu.cn*

5 *Institute for Risk and Reliability, Leibniz University of Hannover, 30167 Hannover, Germany.*

6 *The University of Liverpool, Institute for Risk and Uncertainty, Peach Street, L69 7ZF Liverpool, United Kingdom*

7 *Tongji University, International Joint Research Center for Engineering Reliability and Stochastic Mechanics, Shanghai 200092, China*

Abstract: The collapse risk of building structures has been one of the major factors causing casualties and huge economic losses for earthquake disaster prevention. This paper presents a shaking table test on low-rise steel moment frames with consideration of mass irregularity in the elevation direction. The frames are subjected to naturally observed and artificial seismic waves. As indicated from the test results, the specimen with the irregularity of additive-mass (additional 5% of the roof mass) on the top floor showed considerable amplification on the acceleration and drift responses at the bottom storey when subjected to over-design earthquakes. A numerical model with degraded stress-strain relation is built in terms of fiber elements and calibrated by test results. Incremental dynamic analyses are performed to evaluate the probabilities exceeding three limit states related to immediate occupancy, life safety, and collapse prevention. The seismic fragility curves through a suite of near-fault ground motions in the Uemachi area of Osaka are obtained for the numerical models with and without mass irregularity on the roof, and the vertical mass irregularity tends to play significant roles in the seismic design for collapse prevention.

Keywords: Steel moment frame; Shaking table test; Additive mass; Seismic collapse; Strength degradation; Uncertainty quantification.

1. Introduction

In recent decades, earthquake disasters evoked catastrophic consequences in different regions of the world. These catastrophes are ranging from human casualties, social crises due to the destruction of infrastructure and housing to economic losses. The past Hyogoken-Nanbu earthquake 1995, Chichi earthquake 1999, and Wenchuan earthquake 2008 resulted in enormous civilian deaths, in which 85 % were approximately caused by collapsed buildings. Since then, the problem of seismic collapse for structures became a critical topic in earthquake engineering.

Among various types of structural systems in buildings, the steel moment-resisting frame is a rectilinear assemblage of rigid connections between the steel beam and column components to sustain horizontal loadings. The special steel moment-resisting frames (SMRF) are designed to demonstrate ductile seismic behavior with considerable plastic deformation in beam and column components. However, brittle and fatigue fractures in beam-to-column connections and the local buckling of columns resulting in storey collapse occurred during the great earthquakes (Northridge earthquake 1994 and Hyogoken-Nanbu earthquake 1995).

Concerning the earthquake-induced collapse scenarios of steel moment frames, a generic side-sway collapse mode has been found by Lignos et al. (2011), who experimentally investigated a 4-storey low-rise steel moment frame subjected to incremental earthquake loading. The P-Δ effect and component deterioration in strength and stiffness was found to be dominant factors to trigger asymmetric response before the ultimate collapse. The side-sway collapse is also theoretically explained by a drift concentration at lower stories of high-rise buildings due to the cumulative axial force on beam-columns and its interaction with bending moment strength (Ji et al. 2009; Kim et al. 2009; D'Alessandro et al. 2018; and Bai et al. 2020). However, it was found in the low-rise steel moment frames with 4 storey levels, that the side-sway collapse is likely to occur only at the bottom story using the noncompact cross-section

of columns vulnerable to local buckling (Suita et al. 2008; Bai and Lin 2015). It is thus necessary to further clarify the soft-storey collapse mechanism of 3-4 storey steel moment frames, particularly under the unfavourable direction of earthquake loading through experimental and numerical investigations.

Various seismic testing methods have been developed, such as shaking table tests and hybrid simulation. Carpio, Mosqueda, and Lignos (2016) experimentally evaluated the seismic collapse of a steel moment frame subassembly aiming to provide an efficient testing method on large-scale frame subassemblies instead of large to full-scale shaking table test because very limited facilities enable to test large/full-scale frame systems to collapse (Suita et al. 2008; Yamada et al. 2008). On the other hand, due to the limited capacities of the laboratory, a series of small-scale shaking table tests were performed for evaluating the collapse failure mode of low-rise steel moment frames (Lignos et al. 2011).

Various research studies have been investigated on the seismic performance of frames equipped with mass irregularity to evaluate the influence of non-structural components on the seismic response (Sackman and Kelly 1979; Kelly and Tsai 1985; Tremblay and Poncet 2005; Wang et al. 2018; Bi et al. 2019). The main findings indicated that the mass irregularity played an insignificant impact on the seismic performance of structures and using dynamic seismic design can improve the seismic performance to a limited extent. Nonetheless, when the intensity of earthquakes exceeds the design level, the steel moment frames would face severe damages and even collapse failure. The mass irregularity might become an influential factor for assessing the seismic collapse probability under over-design seismic excitations.

This study focuses on soft-storey collapse probability of low-rise steel moment frames with a mass irregularity equipped on the top under over-design earthquakes. The influence of the mass irregularity in elevation on the collapse capacity is quantified by the fragility curves considering the epistemic uncertainty due to the intensity of ground motions. This paper is

organized as follows: the shaking table test is introduced from the design and fabrication of specimens with and without mass irregularity, loading protocol, and measurements. Thereafter, the dynamic property is characterized by the pure frame and compared with the irregular one to demonstrate the difference in mode shape. The soft-storey collapse is then analyzed based on plasticity theory and incremental dynamic simulations. Finally, the influence of the mass irregularity on multiple levels of damage limit-states is quantified in terms of the fragility analysis.

2. Shaking table substructure tests

2.1 Test specimen

Various seismic testing methods have been developed, such as shaking table tests and hybrid simulation. For instance, Carpio et al. (2016) experimentally evaluated the seismic collapse of a steel moment frame subassembly aiming to provide an efficient testing method on large-scale frame subassemblies instead of large to full-scale shaking table test because very limited facilities enable to test large/full-scale frame systems to collapse (Suita et al. 2008; Yamada et al. 2008). On the other hand, it is a rational way to conduct small-scale shaking table tests for evaluating the collapse failure mode of low-rise steel moment frames (Lignos et al. 2011).

The prototype structure is a single-span four-story steel frame structure. Its plane size is 8m ×8m, the storey height is 3.15m, and the total height of the structure is 12.85m. The mass of the first three floors is 42.5tons, and the top floor is 38.5tons. The cross-sectional specification of the beam and column is H500×225×30×40mm, and the steel is Q345. The height of the equipment is 1.5m. The cross section of the equipment is a circular steel tube design, the outer diameter is 200mm and the wall thickness is 17.5mm. The mass is 2.25ton, which is 5.84% of the floor. The experimental model is designed according to the similarity theory, the scale ratio is 1: 5, and the model-prototype similarity coefficients of each parameter are shown in Table 1.

Table 1 The model-prototype similarity coefficients of parameters

Parameters	Similar relationship	Similarity coefficient
Length	l	1/5
Time	$\sqrt{l}$	$\sqrt{5}/5$
Mass	l^2	1/25
Force	l^2	1/25
Stress	1	1
Strain	1	1
Acceleration	1	1

Fig. 1 shows the elevation views in the strong axis of columns and weak column axis, and tri-dimensional view, respectively. The column distance of the test model structure is 1.6m and the total height of the specimen is 2.57m, including that of the bottom story as 0.68m, and 0.63m for the upper three stories. The floor masses with 1700 kg are applied on respective floors between the bottom and third stories, and the fourth story was applied 1540kg for vertical load and an additional 90 kg equivalent to equipment. The additive-mass is represented by a circular steel thick plate fixed by a vertical steel tube on the roof centroid to eliminate the eccentricity problem during the uni-directional earthquake loadings. The bottom of the steel pipe is welded with the square steel plate. Four bolt holes reserved in the steel plate are used to connect with the steel frame floor.

The selected earthquake waves were input along the lateral axis as shown in Fig. 1(d), which corresponds to the weak axis of columns aiming to reproduce the column collapse scenario of SMRFs under the unfavorable case of seismic excitations. To sustain vertical load at each floor, cross beams are fabricated and welded to the web of the perimeter beams in the middle of the span. The detailed material and geometric properties of beam and column components are presented in Table 2.

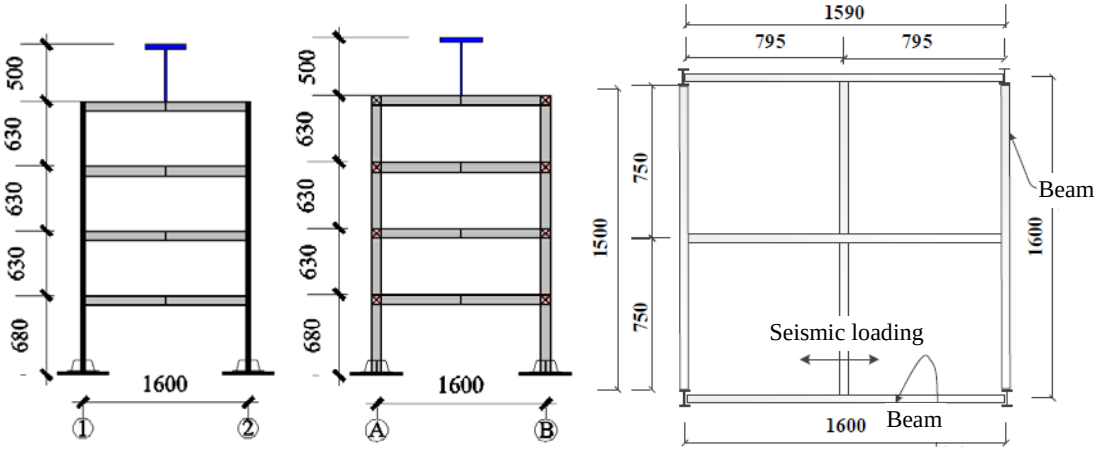

(a) Elevation views in bi-axis (b) Plain view

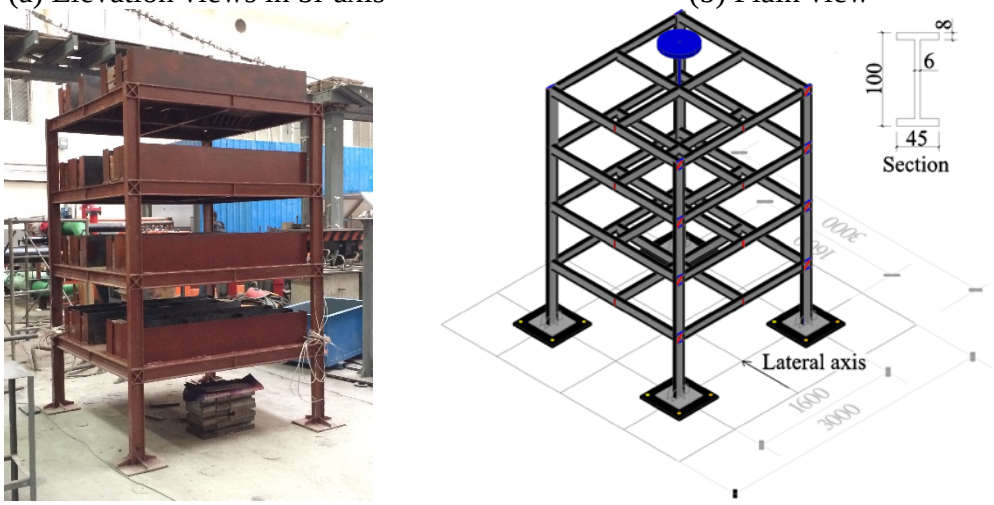

(c) Frame specimen (d) Aerial view of shaking table

Fig. 1 Dimension of the four-story steel moment frame with mass irregularity in blue

Table 1 Material and geometric properties of beam and column components

Component	Material	Section (mm)	Length (mm)	Connection
Columns	Q235	H100×45×6×8	2570	-
Perimeter beams at A-B axis	Q235	H100×45×6×8	1590	$b \times h$ = 19.5 mm × 84 mm Thickness: 8mm
Perimeter beams at 1-2 axis	Q235	H100×45×6×8	1500	$b \times h$ = 19.5 mm × 113 mm Thickness: 8 mm
Cross-beam in the longitudinal axis	Q235	H100×45×6×8	1590	Thickness: 10mm
Cross-beam in the lateral axis	Q235	H100×45×6×8	790×2	Thickness: 10mm

The beam and column components are welded to fabricate the SMRF specimens, and the constructional details of beam-to-column connections, welded beam-beam joints, and fixed column bases are presented in Fig. 2. Stiffeners are placed around panel zones, in which two plates ($b \times h$ = 19.5 mm × 84 mm) sustain the horizontal forces transferred from beam flanges,

and the other two ($b \times h$=19.5mm×113mm) in diagonal directions improve shear resistance of panel zones. The beam flanges are welded on the column flange using a fully penetrated fillet weld with the access hole, as shown in Fig. 2(a). On the other side of the connection, perimeter beams in the lateral direction are welded with similar details along the neutral axis of the column web, as shown in Fig. 2(b). Moreover, the flanges between perimeter beams and cross beams are connected through butt weld on double sides.

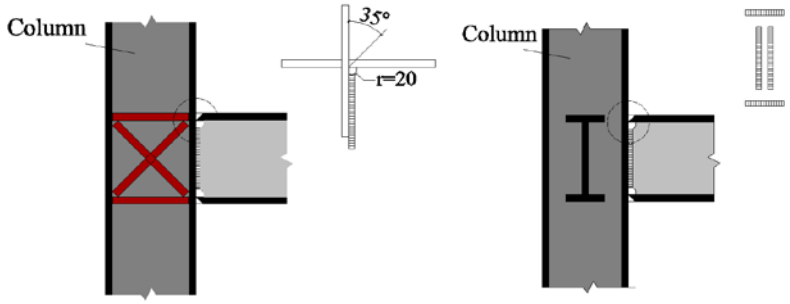

(a) Beam-to-column connections

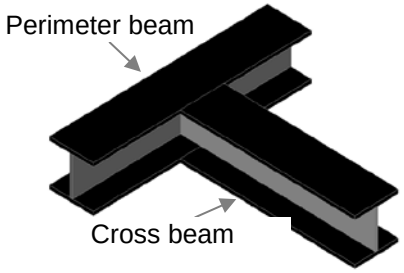

(b) Beam connection

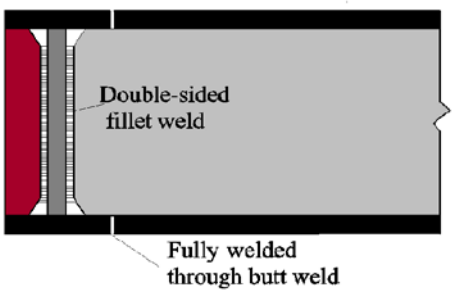

(c) Weld detail

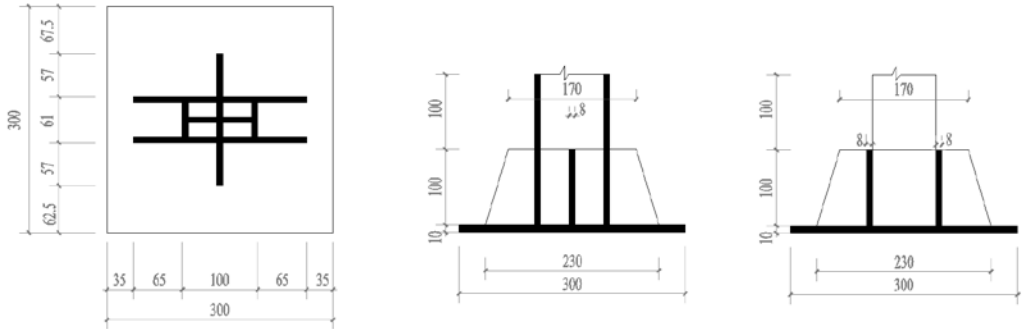

(d) Fixed column bases

Fig. 2 Fabrication of frame specimens

The column slenderness ratio is an important parameter in the seismic design of the structure. The limit of the slenderness ratio can control the overall instability of the structure. According to the limit of slenderness ratio specified in article 8.3.1 of code for seismic design of buildings,

the calculation formula and results of slenderness ratio limit of steel frame structure are shown in Table 3. And the slenderness ratio of column members in the test model is shown in Table 3.

Table 3 Slenderness ratio of columns in each storey

Components	Aspect ratio	Limit calculation formula	Limit
Columns of 1st storey	15.6	$100\sqrt{235/f_y}$	82.53
Columns of other stories	14.4	$100\sqrt{235/f_y}$	82.53

The width-thickness ratio of the steel frame beam and column can ensure that the members will not be partially unstable. According to the limit value of width thickness ratio specified in article 8.3.2 of code for seismic design of buildings, the calculation formula, and results of width thickness ratio limit value of steel frame structure are shown in Table 4. The width-thickness ratios of the beam and column of the test model are shown in Table 4. Moreover, the added mass is applied by placing iron blocks distributed on the slab of each floor with 10 cm in thickness.

Table 4 The width-thickness ratios of components

Components	Plate position	Width-thickness ratio	Limit calculation formula	Limit
Columns	Flange	5.6	$12\sqrt{235/f_y}$	9.9
	Web	14	$48\sqrt{235/f_y}$	39.6
Beams	Flange	5.6	$10\sqrt{235/f_y}$	8.3
	Web	14	/	/

2.2 Input waves and measurement

Before the test, white noise scanning was carried out. The frequency and damping ratio of the structure are obtained by spectral analysis. The natural period of SMRF is 0.42s, and the damping ratio of SMRF is 0.02. The input waves are categorized to be two levels of intensity

corresponding to the maximum capacity earthquakes (Level 1) and over-design earthquakes (Level 2) controlled by the intensity measure of peak ground acceleration (PGA), as shown in Fig. 3, the PGA of level1 is 0.7m/s2 and the PGA of level2 is 2m/s2. Table 5 summarizes the main parameters of three input waves (El-Centro, Synthetic, and Tianjin), i.e. PGA, and Sa (T1, 2%). Moreover, in comparison with the design spectra with the probabilities of occurrence of 63 % and 2 % in 50 years, the spectral acceleration Sa (T1, 2%) of each input wave indicates that the Tianjin wave may excite the maximum responses at the first mode of tested SMRFs. The maximum horizontal seismic impact coefficients of the design spectra are 0.16 and 0.9. Regarding the measurements, horizontal displacement transducers are placed on each floor, and strain gauges are attached on the column ends of the bottom storey. Additionally, a total of 14 accelerometers are used to measure the time-history acceleration responses of each floor.

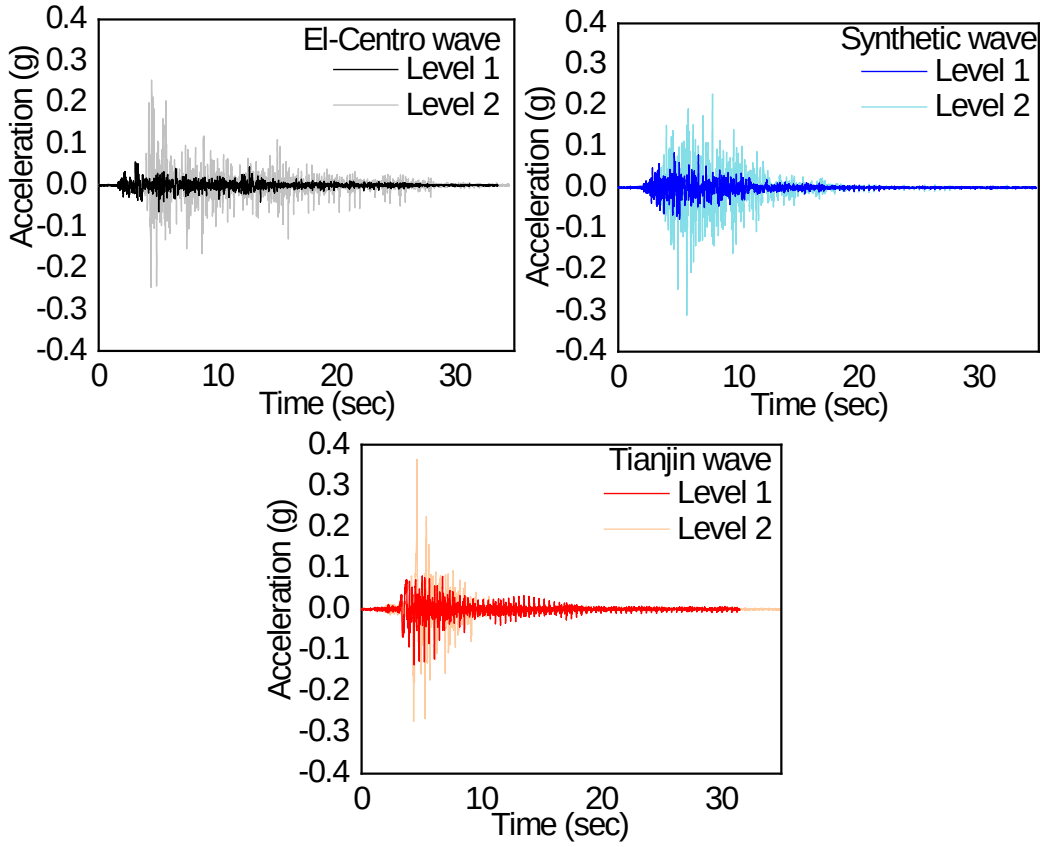

Fig. 3 Acceleration time history of input waves

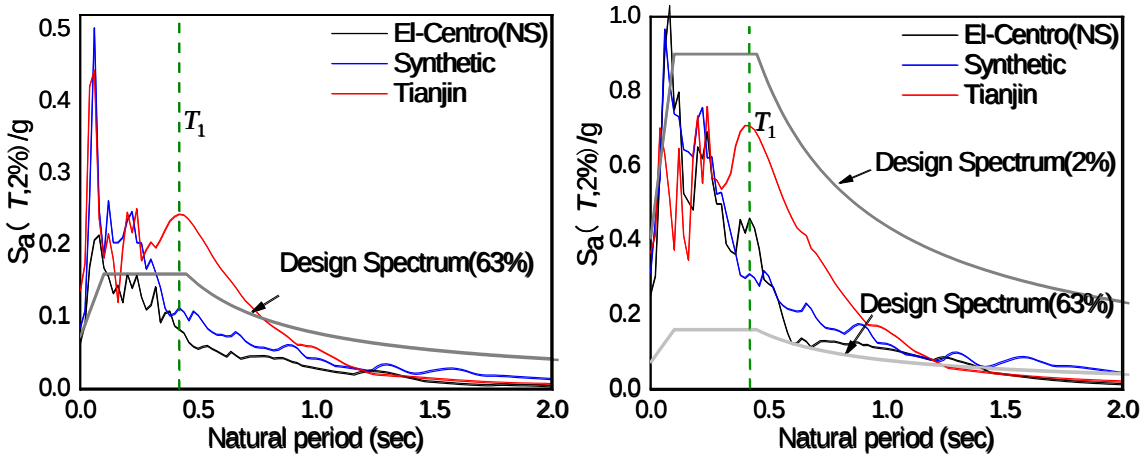

(a) Level 1 earthquakes (b) Level 2 earthquakes

Fig. 4 Acceleration response spectra of input waves

Table 2 Earthquake loading protocols for shaking table test

Earthquake level	Input waves	Peak ground acceleration PGA (gal)	S_a (T_1, 2%)	Specimen
Level 1	El-Centro wave	63.80 gal	0.083	Regular SMRF
	Synthetic wave	84.60 gal	0.113	
	Tianjin wave	135.51 gal	0.243	
Level 2	El-Centro wave	253.80 gal	0.458	Regular SMRF
	Synthetic wave	310.93 gal	0.309	
	Tianjin wave	364.46 gal	0.707	
Level 1	El-Centro wave	111.95 gal	0.142	Irregular SMRF-EM
	Synthetic wave	85.94 gal	0.097	
	Tianjin wave	132.45 gal	0.244	
Level 2	El-Centro wave	144.78 gal	0.185	Irregular SMRF-EM
	Synthetic wave	334.74 gal	0.296	
	Tianjin wave	357.69 gal	0.716	

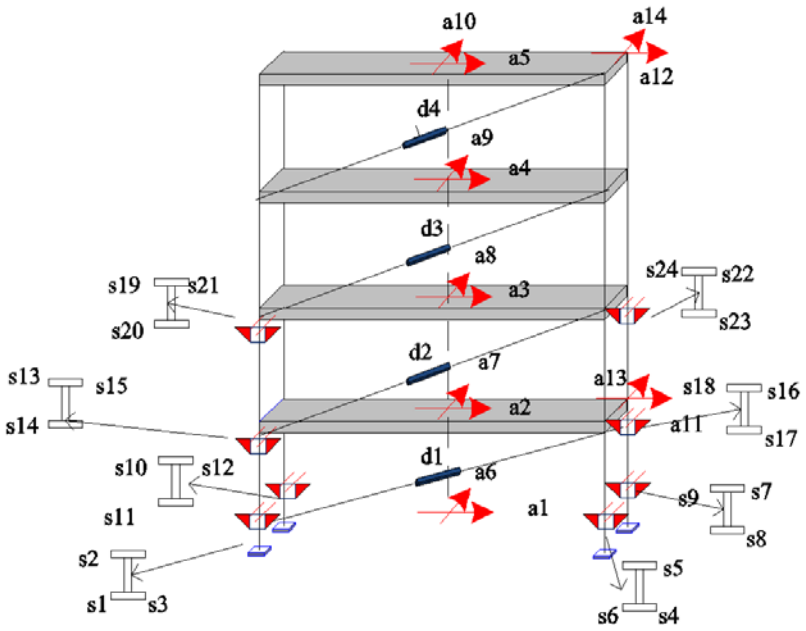

Fig. 5 Displacement transducer, accelerometer, and strain gauge measurements

3. Test results and discussion

3.1 Acceleration responses

Fig. 6 shows the acceleration response spectra of each floor of the regular SMRF and the comparative irregular SMRF-EM. The black dotted line means the acceleration spectrum for the input El-Centro wave, and the solid lines highlighted with various colors are the acceleration spectra corresponding to various floors in elevation. The spectrum of each floor of the two structural systems has an amplification effect compared to the ground spectrum. However, the amplification of the reaction of each floor of SMRF-EM is more obvious, which indicates that the added mass increases the acceleration response of the floors.

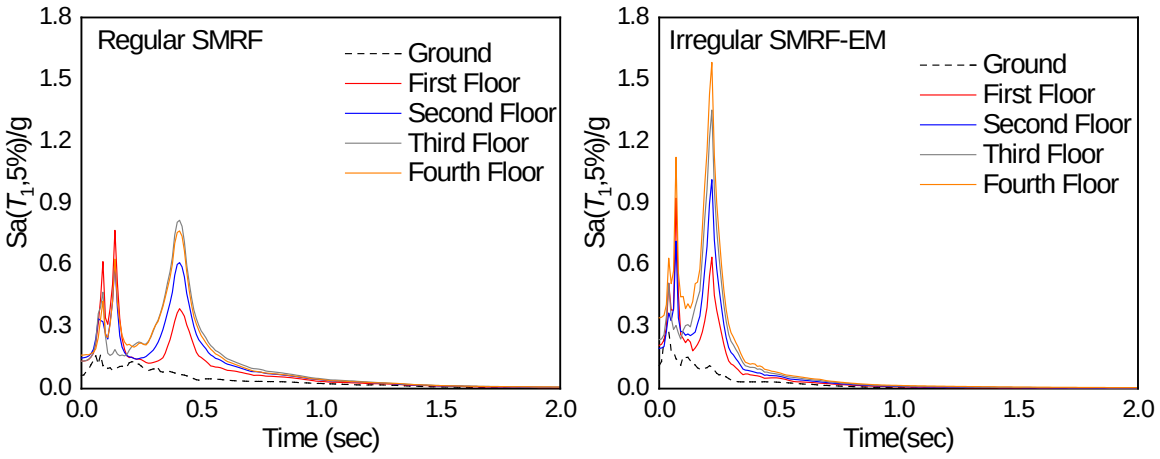

Fig. 6 Acceleration response spectra of each floor under El-Centro wave of Level 1 intensity

To analyze the acceleration response of the structure, a parameter acceleration amplification factor is introduced. The acceleration amplification factor η of each measurement point is equal to the acceleration peak value at that point divided by the ground acceleration peak value. In Figure 7 (a) the acceleration amplification factor for each storey of the SMRF and three different input waves is depicted. Fig. 7 (a) refers to the level 1 intensity according to Table 2, Fig. 7 (b) to the Level 2 intensity. The same information is shown in Figure 8 (a) & (b) for the SMRF-EM.

Fig. 7 and Fig. 8 show that the acceleration amplification coefficient values of each floor under the three seismic waves of level 1 intensity have no similar change trend, indicating that the structure can withstand similar earthquakes. This suggests that the seismic energy is mainly dissipated by the internal damping of the structure. Under the three seismic waves of the level 2 intensity, the variation trend of the acceleration amplification factor is consistent, and the acceleration amplification factor becomes lower, which is caused by the stiffness degradation and the damping ratio increase.

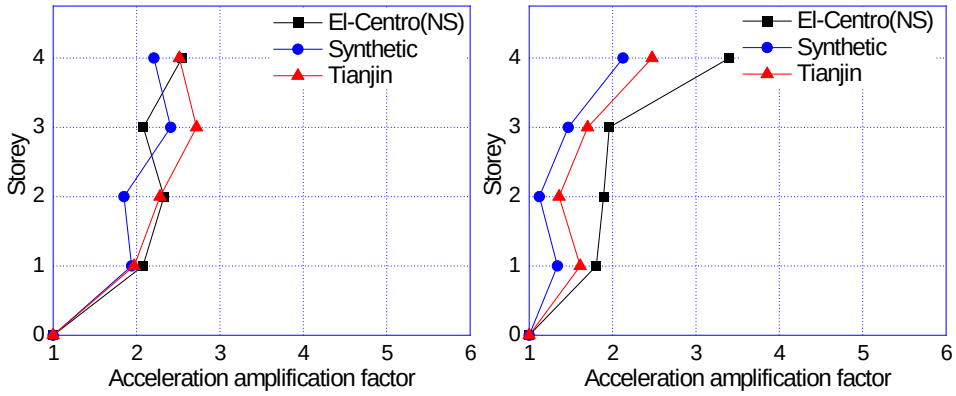

(a) Level 1 earthquake (b) Level 2 earthquake

Fig. 7 Acceleration amplification factor of regular SMRF

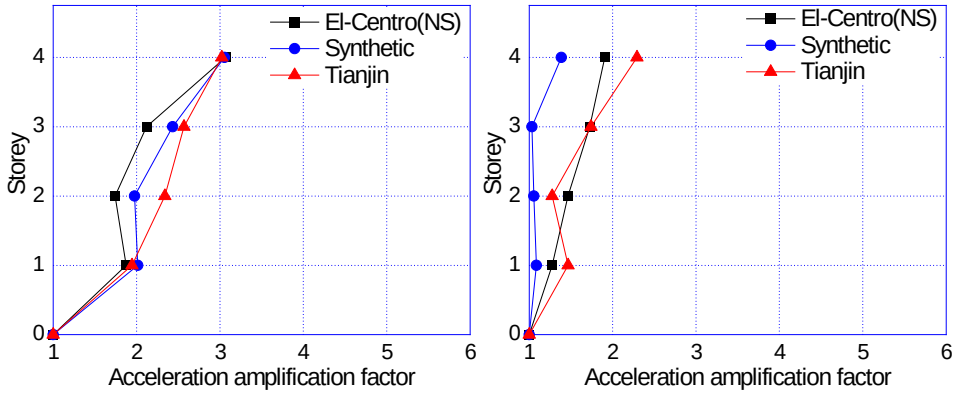

(a) Level 1 earthquake (b) Level 2 earthquake

Fig. 8 Acceleration amplification factor of irregular SMRF-EM

Fig. 9 shows the average value of the acceleration amplification factors for the two structural systems at the level 1 and level 2 intensities. The black line is SMRF and the blue line is SMRF-EM. Under the level 1 intensity earthquake, the additive mass has a great influence on the top-level acceleration. Under the level 2 intensity earthquake, plasticity and damage appear in the structure, and the additive mass even reduces the structural acceleration response.

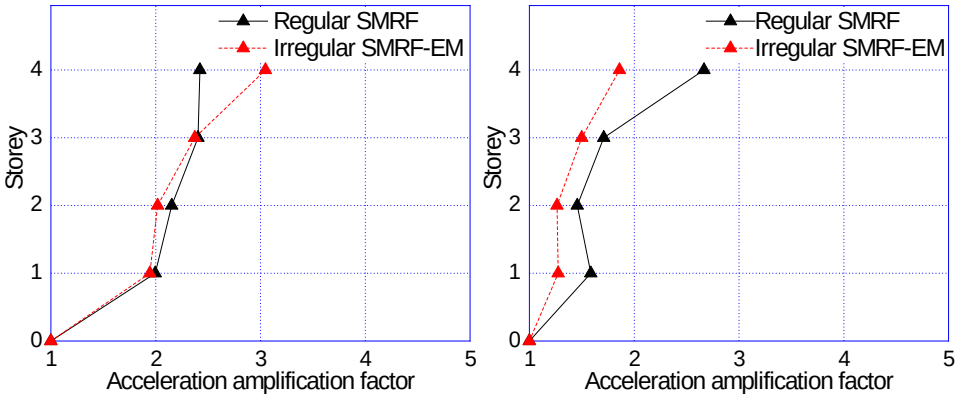

(a) Level 1 earthquake (b) Level 2 earthquake

Fig. 9 Average acceleration amplification factor of regular SMRF and irregular SMRF-EM

3.2 Inter-storey drift ratio

As shown in Fig. 10, under the level 1 intensity earthquake, the inter-storey drift ratio is roughly a linear curve, and the displacement curve of the SMRF is close to a parabola, indicating that the structural deformation is mainly shear deformation, and the SMRF is in the elastic phase at this time. As shown in Fig. 11, under the level 2 intensity earthquake, the inter-storey drift ratio is no longer linear, and there is a significant transition on the second floor of the curve, and the displacement of the first floor is significantly increased. A certain degree of damage and large plastic deformation occurred at the bottom of the SMRF. As shown in Fig. 12, after placing an additional mass that affects the structural response and the displacement response of the structure has changed. Especially under the level 2 intensity Tianjin wave, the inter-storey drift ratio and displacement curve of SMRF-EM exhibit excessive responses at the bottom storey which are greatly exceeding the collapse limit.

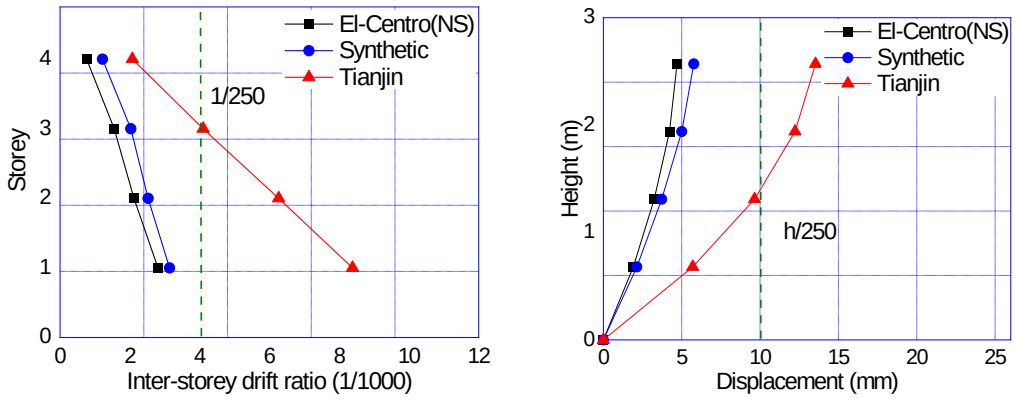

(a) Inter-storey drift ratio (b) Horizontal displacement

Fig. 10 Storey and overall responses of regular SMRF under level 1 earthquakes

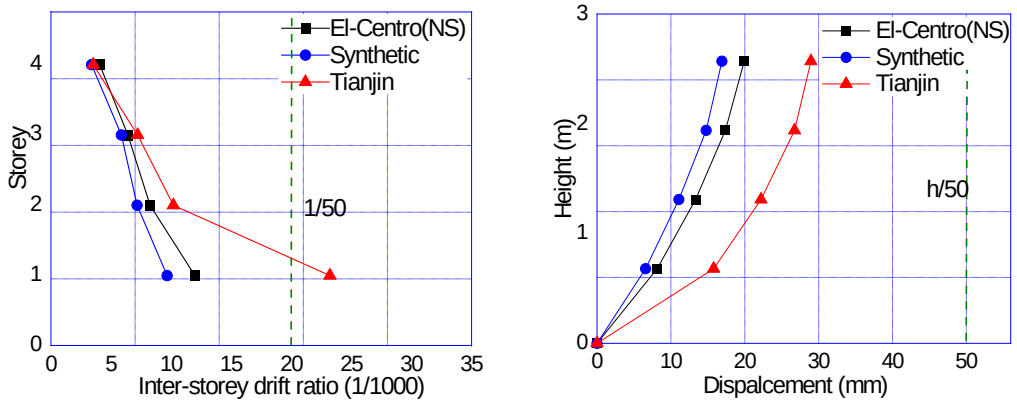

(a) Inter-storey drift ratio (b) Horizontal displacement

Fig. 11 Storey and overall responses of regular SMRF under level 2 earthquakes

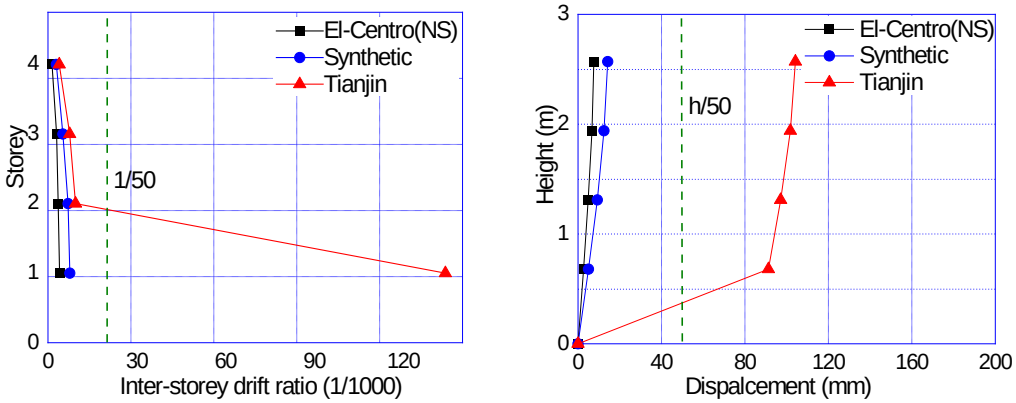

Fig. 12 Storey and overall responses of irregular SMRF-EM under level 2 earthquakes

The inter-storey drift ratio and the horizontal displacement mean of SMRF and SMRF-EM are compared, as shown in Figs. 13 and 14. Under the level 1 intensity earthquake, The results of each floor of SMRF-EM are slightly larger than those of SMRF. Under the level 2 intensity earthquake, The results of the first floor of the SMRF-EM increased significantly, and the remaining floors were slightly reduced. Therefore, we can infer that the device has some influence on the seismic response and even on the collapse behavior of the structure.

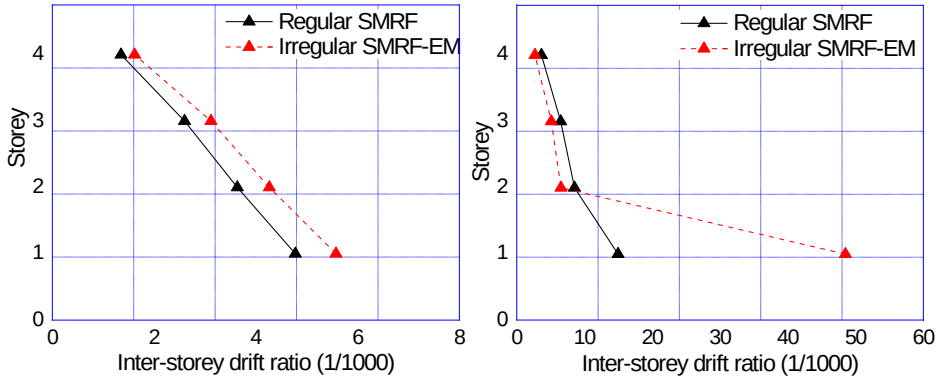

(a) Level 1 earthquake (b) Level 2 earthquake

Fig. 13 Comparisons on average responses of regular SMRF and irregular SMRF-EM

3.3 Component strains

The experiment uses H-beam steel with a yield strength of 339.6 MPa and an elastic modulus of 206 GPa, and the yielding strain is 1648×10e-6. Table 2 shows the strain peaks at the bottom of the first-floor column of the A-axis column. Under the level 2 intensity earthquake, all the strains of the SMRF-EM first floor column have exceeded the strain gauge range, so no strain value was measured. It can be seen from Table 2 that the maximum tensile strain at the 1 and 2 measuring points of the column section and the maximum compressive strain at the 3 measuring points occur simultaneously under the Level 1 EL-Centro and synthetic waves. It can be stated that the member remains still in the elastic phase, and the stress on the section is linear. When the intensity is increased to level 2, the part of the micro-strain peak is larger than the yielding strain, and the maximum tensile strain of the measured point is greater than the maximum compressive strain of the measuring point, indicating that the member has entered the plastic stage at this time and the deformation increases.

Table 2 Peak strain responses (10^{-6}) at the column bottom of the first storey at 1-A axis

	El-Centro wave			Synthetic wave			Tianjin wave		
	s1	s2	s3	s1	s2	s3	s1	s2	s3
Regular SMRF (Level 1)	576	504	457	672	596	581	1923	1492	1356
	-490	-424	-532	-613	-546	-623	-1367	-1425	-1701
Regular SMRF (Level 2)	2002	1936	1569	1746	1671	1152	3105	3158	1796
	-2043	-1989	-1550	-1434	-1364	-1393	-2578	-2632	-2102

Irregular SMRF-EM	986	920	792	750	714	575	1492	1439	1362
(Level 1)	-900	-849	-845	-639	-615	-657	-1543	-1492	-1306

Table 3 Peak strain responses (10^{-6}) at various locations of 1-A axis under the synthetic wave

	Column bottom 1st storey			Column top 1st storey			Column top 2nd storey		
	s1	s2	s3	s13	s14	s15	s19	s20	s21
Regular SMRF	672	596	581	592	565	627	428	447	488
(Level 1)	-613	-546	-623	-579	-604	-578	-522	-552	-393
Regular SMRF	1746	1671	1152	*	1815	1981	1024	1107	1248
(Level 2)	-1434	-1364	-1393	*	-2246	-1621	-1304	-1394	-987
Irregular SMRF-EM	750	714	575	*	645	740	474	521	551
(Level 1)	-639	-615	-657	*	-728	-643	-572	-649	-438
Irregular SMRF-EM	-	-	-	*	-	17633	986	1108	1124
(Level 2)	-	-	-	*	-	-	-1171	-1313	-920

4. Seismic collapse simulations

4.1 Modal analysis

When a multi-degree-of-freedom (MDOF) system is subjected to an earthquake wave, its dynamic equivalence can be formulated by

$$m\ddot{u} + c\dot{u} + ku = -m\ddot{u}_g . \tag{1}$$

Assume the vibration system is without damping, then $\ddot{u}_g = 0$, $c = 0$, Eq. (1) becomes

$$m\ddot{u} + ku = 0 . \tag{2}$$

Then, the displacement u can be solved in terms of $u = \phi \sin(\omega t + \varphi)$, which is equivalent to the following equation:

$$(k - \omega^2 m)\phi = 0 , \tag{3}$$

where ω is natural frequency, the frequencies of each mode ω_i, and the associated eigenvectors ϕ_i can be obtained. The vibration mode of structures is dependent on the degree of freedom, and the structural deformation can be presented as a linear combination of various modes as:

$$u = \sum_{n=1}^{N} q_n \phi_n . \tag{4}$$

Substitute Eq. (4) into Eq. (1), we can obtain the following equations:

$$m\sum_{n=1}^{N}\phi_n\ddot{q}_n + c\sum_{n=1}^{N}\phi_n\dot{q}_n + k\sum_{n=1}^{N}\phi_n q_n = -m\tau\ddot{u}_g, \quad (5)$$

$$M_n\ddot{q}_n + C_n\dot{q}_n + K_n q_n = -\phi_n^T m\tau\ddot{u}_g. \quad (6)$$

Introduce the mode participation factor $\Gamma_n = \frac{\phi_n^T m\tau}{M_n}$, then above equations become:

$$\ddot{q}_n + 2\xi_n\omega_n\dot{q}_n + \omega_n^2 q_n = -\Gamma_n\ddot{u}_g. \quad (7)$$

According to the distribution of earthquake force determined by $s = m\tau$, the contribution of the *n*-th mode on *s* can be presented below:

$$s_n = \Gamma_n m\phi_n. \quad (8)$$

The contributions of the first mode for the steel moment frames with and without additive mass are 93.72% and 93.32% respectively, indicating that the additive mass plays a minor role in the vibration modes. However, the second mode of the steel moment frame with additive mass demonstrates an abnormal vibration shape forming a whipping effect. Although its contribution is negligible (0.86%), the influence might be amplified when extensive redistribution of forces occurs during the formation of the collapse mechanism. The first to fourth mode shapes of those two types of SMRFs are demonstrated in Fig. 14.

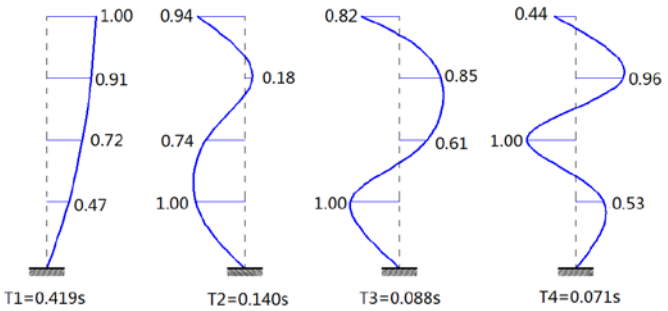

(a)

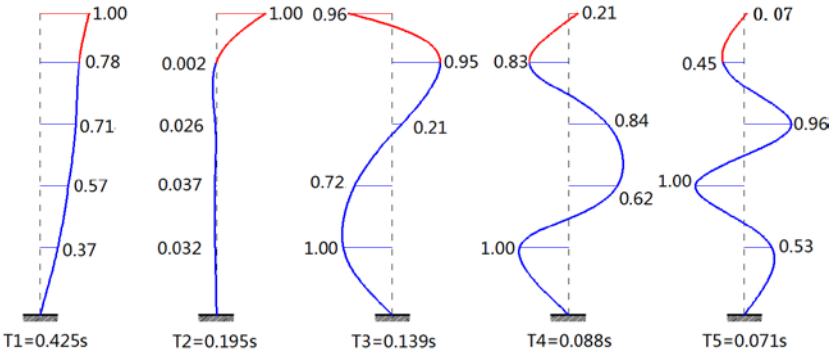

(b)

Fig. 14 Natural mode shapes of various frames: (a) Vibration modes of regular SMRF, (b) Vibration modes of irregular SMRF-EM

4.2 Numerical simulations

For simulating the seismic responses of SMRF models, the beam and column components are modeled by the displacement-based beam-column fiber element with plastic hinges. The beam-column section is divided into fiber layers with 174 discretizations. Particularly, each flange is subdivided into 15×3 blocks equal to a total of 45 elements, and the web is divided into 4×21 blocks with a total of 84 elements. The additive mass element adopts a circular steel tube with 8 and 2 layers in the circumferential direction and the radial directions. The vertical mass is concentrated on the center of each floor, and the additive mass is placed on the center of the frame roof. The vertical loads associated with those masses are uniformly applied on beam elements in static loading protocol. The column bases are fixed with the foundation, and the damping ratio of 0.02 is used for frames. The implementation of the constraint equation in the analysis (constraints) is transformation. The degree of freedom is optimized based on the RCM algorithm. The Newton-Raphson iteration method was employed to control the convergence, the tolerance of which is defined to be 10e-5 in terms of energy absorption. The Newmark-β method was adopted for the stepwise integration of nonlinear dynamic analysis.

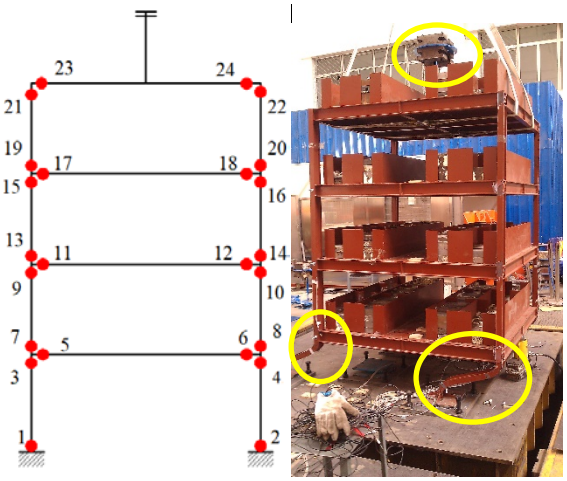

Fig. 16 Fiber element modeling and collapse failure scenario of the tested specimens

The skeleton stress-strain relation for the fiber element of steel materials is characterized by a tri-linear envelope in compression and tension directions. The skeleton curve is determined by critical stress and strain at the turning points of each linear, such as the stresses (σ_{t1}, σ_{t2}, σ_{t3}, σ_{c1}, σ_{c2}, and σ_{c3}) and the associated strains (ε_{t1}, ε_{t2}, ε_{t3}, ε_{c1}, ε_{c2}, and ε_{c3}) as shown in Fig. 17. The hysteretic behavior is controlled by the unloading stiffness coefficient (β), and pinching factor (p_x and p_y) which can be negligible for H-shaped steel components because the pinching effect usually plays a significant role in reinforced concrete structures. For the H-shaped beam and column components under compressive loading, the onset of local buckling occurs at the peak point (ε_{lb}, σ_{lb}), and the following strength degradation can be treated by a negative slope in the skeleton curve. The gradient of this post-capping strength degradation is a significant parameter for collapse simulations, and the critical strain corresponding to the onset of strength degradation should be quantified in terms of the geometric and material properties of the beams and columns. Particularly, the value of ε_{c2} is dependent on the width-to-thickness ratio of flanges (B/T_f), the height-to-thickness ratio of webs [$(D - 2 \cdot T_f) / T_w$], and the yield strain of steel materials ($\varepsilon_{c1} = \sigma_{c1} / E_s$). The following equation about those properties can be used to calculate ε_{c2} of H-shaped steel beam and column components:

$$\varepsilon_{lb} = \max\left[\frac{0.18}{\alpha_f} + \frac{2.6}{\alpha_w} + 0.3, \frac{0.5}{\alpha_f} + \frac{5.7}{\alpha_w} - 4.0\right] \cdot \varepsilon_y, \quad (9)$$

where

$$\alpha_w = \left[(D - T_f)/T_w\right]^2 \cdot \varepsilon_y, \quad \alpha_f = \left(B/T_f\right)^2 \cdot \varepsilon_y. \quad (10)$$

Given the above equations, the critical strain at local buckling can be determined. Thereafter, the remaining stress after the local buckling induced strength degradation (σ_r) can be determined as a ratio of the stress corresponding to critical strain at local buckling (σ_{lb}):

$$\sigma_r = r_{spm} \cdot \sigma_{lb}, \quad (12)$$

where r_{spm} is the ratio related to the geometric parameters as follows:

$$r_{spm} = -0.062\alpha_w - 0.56\alpha_f + 0.98. \quad (13)$$

The corresponding strain can be calculated by the gradient of the negative slope (τ_{lb}):

$$\varepsilon_r = \frac{(r_{spm} - 1)\sigma_{lb}}{\tau_{lb} E} + \varepsilon_{lb}, \quad (14)$$

where

$$\tau_{lb} = -0.0046\alpha_w^2 - 0.57\alpha_f^2 - 0.0005. \quad (15)$$

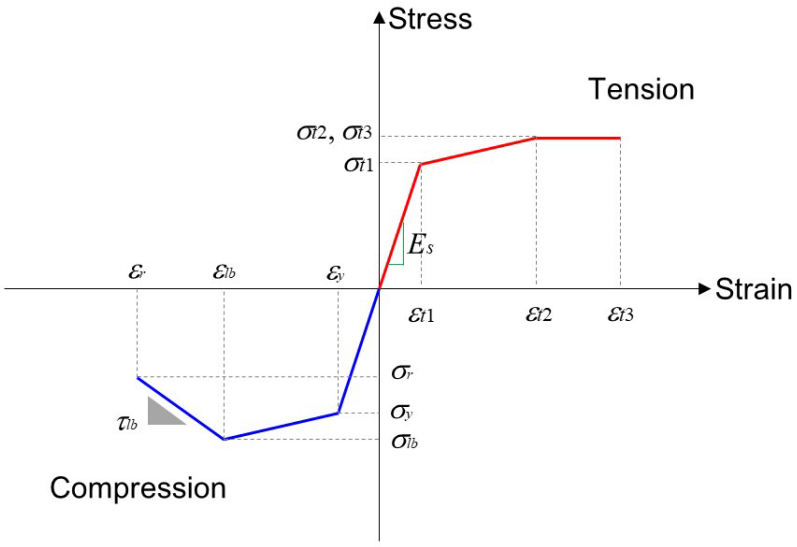

Fig. 17 Stress-strain model for steel fiber elements

The above stress-strain materials model incorporating the post-local buckling strength

degradation was employed for time-history dynamic analyses to calibrate the numerical model by comparing the results with that of the shaking table tests of various SMRFs. Fig. 18 presents the comparisons on the experimental and numerical results of the inter-storey drift ratio and overall displacement for various frames. The numerical results for the regular SMRF demonstrate very good agreement with the experimental ones. Contrarily, a larger discrepancy was found for the irregular SMRF-EM because that soft-storey collapse induces instability at the bottom storey when subjected to the level 2 earthquake of the Tianjin record. Overall, the accuracy of the numerical model with degraded stress-strain relation is proven to be reasonable for incremental dynamic analyses of regular and irregular SMRFs under over-design earthquakes.

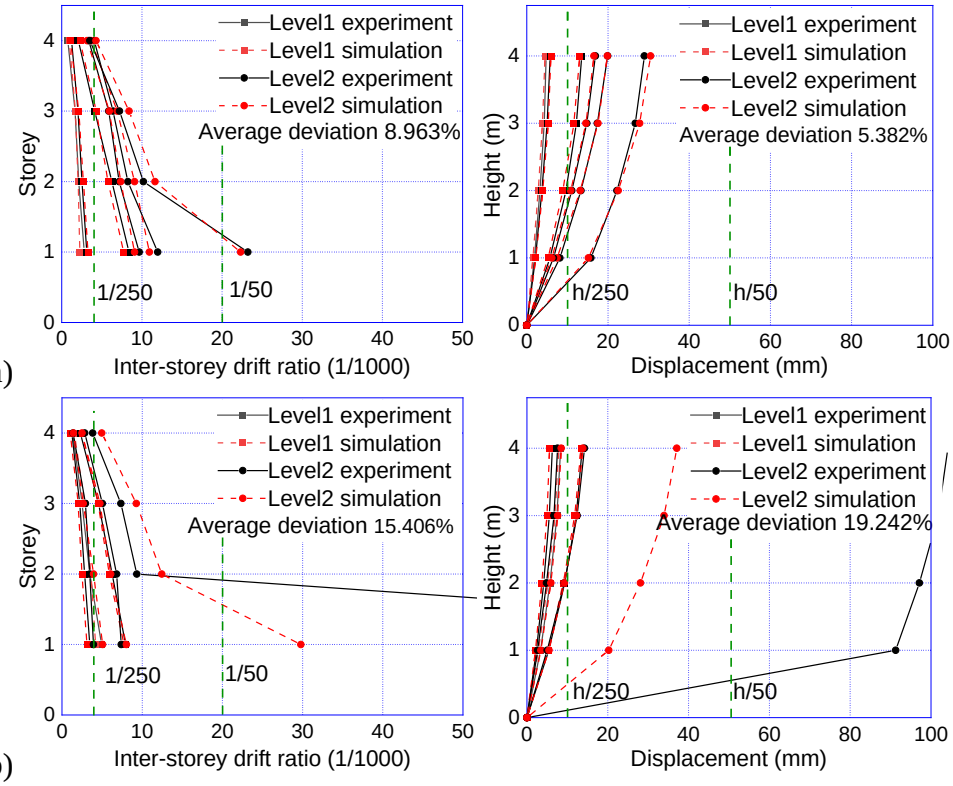

Fig. 18 Experimental and simulation results of inter-storey drift ratio and floor displacement: (a) Regular SMRF, and (b) Irregular SMRF-EM

5. Collapse fragility

5.1 Incremental dynamic analyses

388 This section further evaluates the influence of epistemic uncertainty from the intensity of
389 ground motions on the seismic collapse fragility of regular and irregular SMRFs. The active
390 Uemachi-fault in the Kansai area of Japan has been assessed to face a high probability of
391 occurrence in the future 30 years (S rank), especially under the risks of subduction-zone
392 earthquakes near the Nankai ocean trough. As shown in Fig. 19, the cabinet office, the
393 government of Japan (2010) published the anticipated damages and the seismic intensity scale
394 of the Osaka area when subjected to synthetic Uemachi-fault earthquake (M 7.6). The intensity
395 can be calculated by $I = 2\lg^{a} + 0.94$ where a is the average acceleration in the time domain.
396 The value 7 for I states the highest level of the intensity scale which corresponds to a greater
397 than 30 % collapse ratio of buildings. Moreover, the severe damages are found near the
398 Uemachi-fault where the mainshock is induced, so the near-fault ground motions are mainly
399 focused to evaluate the damage and collapse fragility of low-rise SMRFs with mass
400 irregularity in elevation.

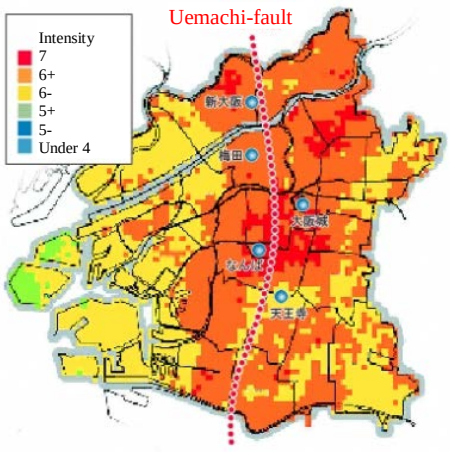

401

402 Fig. 19 Intensity distribution during the Synthetic Uemachi-fault earthquake (in Osaka area)

403 Given the occurrence probability and the induced server damages of this earthquake, the
404 corresponding near-fault ground motions are selected for evaluating the collapse fragility.
405 Table 4 summarizes a suite of artificial waves in EW and NS directions near the Uemachi-
406 fault, and their main parameters (Taga 2011). From the acceleration spectra of those waves as

demonstrated in Fig. 20, the peak responses are larger than the design spectrum. It means that the design spectra with the occurrence probability of 63% and 2% in 50 years underestimate the recorded intensity compared with that of the Uemachi-fault earthquake.

Table 4 Parameters of synthetic Uemachi near-fault ground motions

Area	Component	Name	PGA (g)	PGV (cm/s)
A area	EW	UMT-A02S-EW	0.3873	118.4
		UMT-A03S-EW	0.5244	155.2
		UMT-A04S-EW	0.7362	258.6
		UMT-A05S-EW	0.6368	176.7
		UMT-A08S-EW	0.3208	62.2
		UMT-A09S-EW	0.5215	96.0
		UMT-A10S-EW	0.3535	226.7
	NS	UMT-A02S-NS	0.2619	74.4
		UMT-A03S-NS	0.5310	150.4
		UMT-A04S-NS	0.5480	144.7
		UMT-A05S-NS	0.5063	154.0
		UMT-A08S-NS	0.3352	96.6
		UMT-A09S-NS	0.6205	103.4
		UMT-A10S-NS	0.5512	148.3
D area	EW	UMT-D02S-EW	0.7689	110.0
		UMT-D04S- EW	1.0444	123.1
		UMT-D06S- EW	0.8856	163.2
		UMT-D08S- EW	0.5301	74.4
		UMT-D10S- EW	0.9475	226.6
	NS	UMT-D02S-NS	0.5983	102.6
		UMT-D04S-NS	1.1872	129.7
		UMT-D06S-NS	0.8180	128.5
		UMT-D08S-NS	0.9125	93.0
		UMT-D10S-NS	0.8316	252.0

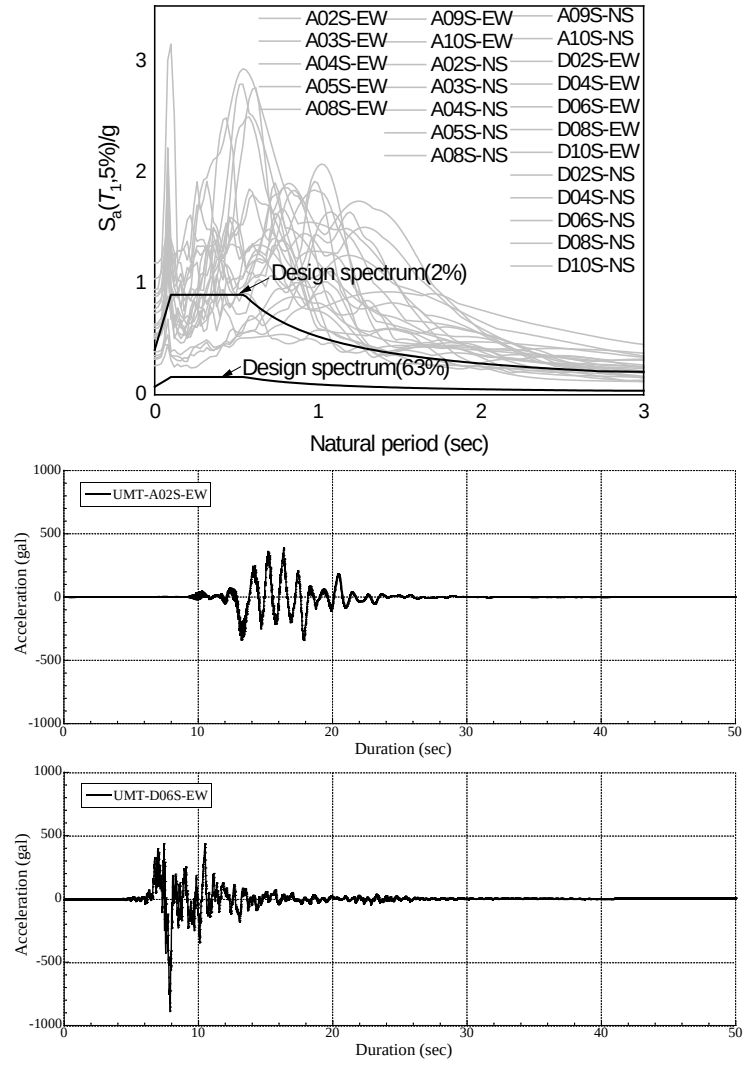

Fig. 20 Characteristics of near-fault waves for the Uemachi fault

5.2 Collapse fragility assessment

The selected Uemachi near-fault ground motions are applied to perform incremental dynamic analyses on regular SMRFs and irregular SMRF-EMs. Elasto-plasticity and strength degradation are accounted for material nonlinearity and softening, and geometric nonlinearity is included to incorporate the P-Δ effect. The intensity of each wave is scaled in terms of PGA to simulate the responses from the range of elasticity to the final collapse. The maximum inter-storey drift ratio (θ_{max}) is treated to be the response indicator used for identifying the limit states for various extents of structural damage. According to the specifications in FEMA356, three limit states are recommended to identify the seismic performances of damaged SMRFs,

i.e. Immediate Occupancy (IO), Life Safety (LS), and Collapse Prevention (CP). The associated values of θ_{max} are 7/1000 rad, 2.5/100 rad, and 5/100 rad. From the results of incremental dynamic analysis for regular and irregular frame models as shown in Fig. 21, the relation between PGA and θ_{max} of each case is derived, and the PGA distribution at the limit states of IO, LS, and CP means the epistemic uncertainty from the individual wave.

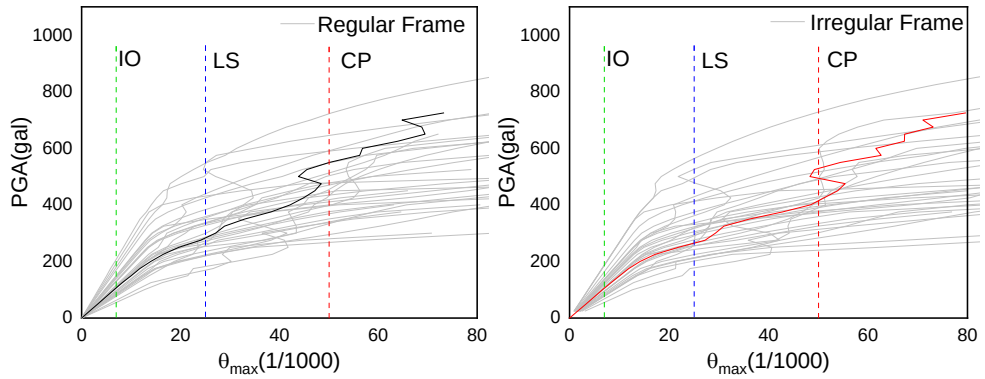

(a) Irregular steel moment-resisting frame (b) Irregular frame with additive mass

Fig. 21 Incremental dynamic analyses of various frames under near-fault ground motions

Based on the PGA distributions corresponding to various limit state, the seismic fragility can be presented by the following equation:

$$\mathrm{F}(x) = P(D > C \mid PGA = x)\,, \tag{16}$$

where F(x) is the fragility function, D is the drift response of structures, C indicates the deformation capacity specified by seismic design demands with respect to various limit states as aforementioned IO, LS, and CP. We assume that the drift responses full normal distribution as follows:

$$\ln D \sim N(\ln \lambda, \zeta)\,, \tag{17}$$

where λ and ζ are mediate value and exponential standard deviation of the seismic response function subjected to certain intensity (PGA) of earthquakes. Accordingly, the seismic fragility is modeled by a lognormal cumulative distribution function as follows:

$$\mathrm{F}(x) = \phi\left[\frac{\ln \lambda - \ln C}{\zeta}\right]. \tag{18}$$

448 The fragility parameters can be estimated by the least-squares regression which minimizes
449 the sum of squared error between the predicted demand and the demand values obtained from
450 incremental dynamic analysis. The demand is represented as a power-law function of the PGA
451 adopting a regression approach:

452 $$\lambda = \alpha \left(\mathrm{PGA}\right)^{\beta}. \tag{19}$$

453 Then, the natural logarithm of nearby two becomes

454 $$\ln\lambda = \alpha + \beta \ln(\mathrm{PGA}), \tag{20}$$

455 where α, β and ζ can be solved in terms of the linear regression from the results of incremental
456 dynamic analysis, as shown in Fig. 22(a). The inter-storey drift ratio (θ_x) can be adopted as the
457 engineering demand parameter to evaluate the probability of failure concerning the seismic
458 intensity PGA. The fragility function for the regular SMRF can be presented by

459 $$\ln(\theta_x) = 1.217\ln(\mathrm{PGA}) - 10.624, \tag{21a}$$

460 where the corresponding standard deviation ζ = 0.442. Then using Eq. (18) will attain the
461 seismic fragility exceeding the limit states of IO, LS, and CP, Fig. 22(b):

462 $$\mathrm{P}_1 = \Phi\left[\frac{1.217\ln(PGA) - 10.624 - \ln(0.007)}{0.442}\right], \tag{22a}$$

463 $$\mathrm{P}_1 = \Phi\left[\frac{1.217\ln(PGA) - 10.624 - \ln(0.025)}{0.442}\right], \tag{22b}$$

464 $$\mathrm{P}_1 = \Phi\left[\frac{1.217\ln(PGA) - 10.624 - \ln(0.050)}{0.442}\right], \tag{22c}$$

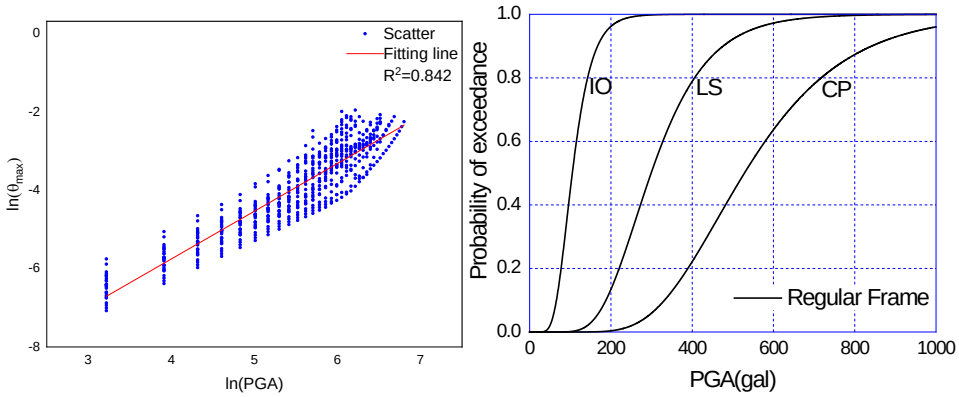

Fig. 22 Fragility analysis of regular SMRF: (a) Regression approach for fragility parameters and (b) Fragility curves for various limit states

Similarly, the fragility parameters for irregular SMRF-EM are presented in the following equation:

$$\ln(\theta_x) = 1.243\ln(\mathrm{PGA}) - 10.718\,. \tag{23}$$

Based on the standard deviation $\zeta = 0.466$, the fragility curves associated with three levels of limit states can be represented as follows:

$$\mathrm{P}_1 = \Phi\left[\frac{1.243\ln(PGA) - 10.718 - \ln(0.007)}{0.466}\right], \tag{24a}$$

$$\mathrm{P}_1 = \Phi\left[\frac{1.243\ln(PGA) - 10.718 - \ln(0.025)}{0.466}\right], \tag{24b}$$

$$\mathrm{P}_1 = \Phi\left[\frac{1.243\ln(PGA) - 10.718 - \ln(0.050)}{0.466}\right], \tag{24c}$$

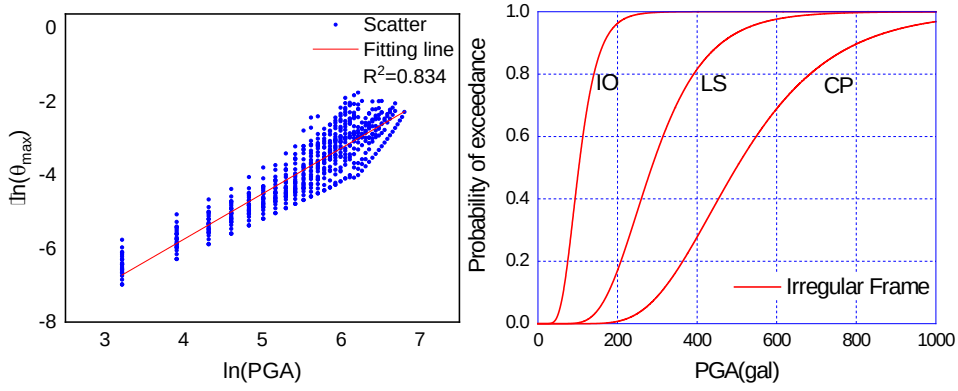

Fig. 23 Fragility analysis of irregular SMRF-EM: (a) Regression approach for fragility parameters, and (b) Fragility curves for various limit states

The seismic fragility of tested regular and irregular SMRFs with and without additive mass can be assessed as the aforementioned approach. It is clear from Fig. 24 that vertical mass irregularity influences the probability of failure exceeding the limit state of CP relative to the IO and LS. The seismic collapse fragility

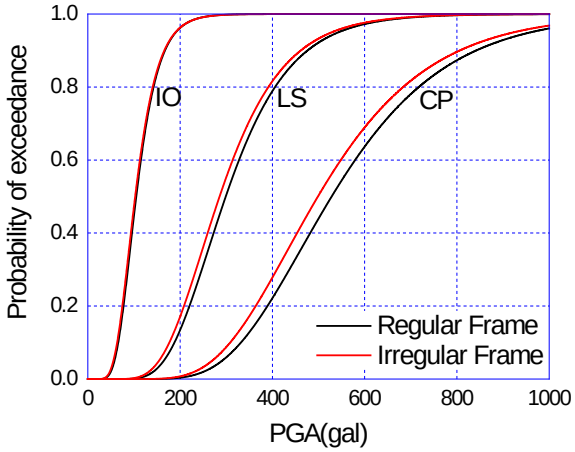

Fig. 24 Fragility curves with respect to various limit states of seismic performance

6. Conclusions

This paper experimentally investigates the seismic collapse scenario of low-rise 4-storey steel moment frames with and without additive mass. Numerical modeling and incremental dynamic analysis using the OpenSees program are performed to quantify the epistemic uncertainty of earthquake characteristics on the collapse probability of low-rise steel moment frames with the storey irregularity generated from the additive mass. The main conclusive remarks are presented as follows:

- Shaking table tests of four-storey SMRFs revealed that the additive mass on the roof of regular SMRFs amplifies the acceleration responses at floors under design level earthquakes, and further enlarges the maximum inter-storey ratio at the bottom storey inducing soft-storey collapse mechanism.
- A numerical model with degraded stress-strain relation is developed for incremental dynamic analyses, in which the post-local buckling strength degradation was incorporated by

a negative slope in compression of H-shaped steel beam and column components. Calibration results indicate that the numerical approach is promising to predict the soft-storey collapse mechanism of low-rise SMRFs under strong earthquakes.

- The selected near-fault ground motions from the Uemachi fault are applied to evaluate the epistemic uncertainty through incremental dynamic analyses on the tested SMRFs with and without additive mass. Fragility curves showed that vertical mass irregularity influences the probability of failure exceeding the limit state of collapse prevention.

Moreover, future studies will be continued to focus on the coupling effect on torsional responses of the irregular SMRFs with additive mass and stiffness in plan and elevation. The aleatory uncertainty caused by the strength degradation should be evaluated to quantify its influences on collapse fragility under over-design earthquakes.

Acknowledgment

This study is partially supported by the Scientific Research Fund of Institute of Engineering Mechanics, China Earthquake Administration (Grant No. 2020EEEVL0413); the Key Laboratory of Urban Security and Disaster Engineering of Ministry of Education, Beijing University of Technology (Grant No. 2021B04); the Fundamental Research Funds for the Central Universities (2020CDJQY-A063), and the Alexander von Humboldt Stiftung-Foundation (1196752).

References

Mahin S A. (1998) Lessons from damage to steel buildings during the Northridge earthquake. *Engineering Structures*, 20(4–6): 261-270.

Bai, Y., Ma, X., Wang, B., Cao, G., and Beer, M. (2020). Cumulative component damages on collapse capacity of ductile steel and CFT moment resisting frames under over-design ground motions. *Journal of Earthquake Engineering*, 16: 1-22.

Paolo Castaldo, P., Amendola, G., and Palazzo, B. (2017). Seismic fragility and reliability of

structures isolated by friction pendulum devices: seismic reliability-based design (SRBD). *Earthquake Engng Struct. Dyn.* 46: 425–446

D'Alessandro, E., De Matteis, G., Brando, G. Design charts for end-plate beam-to-column steel joints (2018) *Proceedings of the Institution of Civil Engineers: Structures and Buildings*, 171 (6), 472-486.

Deniz, Derya, Song, et al. (2017) Energy-based seismic collapse criterion for ductile planar structural frames. *Engineering Structures*, 141:1-13

Ji, X., Kato, M., Wang, T., Hitaka, T., & Nakashima, M. (2009). Effect of gravity columns on mitigation of drift concentration for braced frames. *Journal of Constructional Steel Research*, 65, 2148-2156.

Kim, M., Araki, Y., Yamakawa, M., Tagawa, H., & Ikago, K. (2009). Influence of P-Delta effect on dynamic response of high-rise moment resisting steel buildings subjected to extreme earthquake ground motions. *Journal of Structural and Construction Engineering, 644*, 1861–1867. (in Japanese).

Lignos, D.G., Krawinkler, H., & Whittaker, A. S. (2011). Prediction and validation of sidesway collapse of two scale models of a 4-story steel moment frame. *Earthquake Engineering & Structural Dynamics, 40*, 807–825.

Hwang, S. and Lignos, D. (2017). Earthquake ‐ induced loss assessment of steel frame buildings with special moment frames designed in highly seismic regions. *Earthquake Engineering & Structural Dynamics*, 46(13), 2141-2162.

Suita, K., Yamada, S., Tada, M., Kasai, K., Matsuoka, Y., Shimada, Y. Collapse Experiment on Four-Story Steel Moment Frame: Part 2. *Proc. 14th World Conf. Earthquake Eng*: Beijing, China, 2008.

Sackman, J. and Kelly, J. (1979) Seismic analysis of internal equipment and components in structures. *Engineering Structures*, 1(4), 179-190.

551 Tremblay, R. and Poncet, L. (2005) Seismic Performance of Concentrically Braced Steel
552 Frames in Multistory Buildings with Mass Irregularity. *Journal of Structural Engineering*,
553 131(9), 1363-1375.
554 Wang, J., Dai, K., Yin, Y, Tesfamariam, S. (2018) Seismic performance-based design and risk
555 analysis of thermal power plant building with consideration of vertical and mass
556 irregularities. *Engineering Structures*, 164, 141-154.
557